On the Occurrence of Atmospheric States that are Non-Elliptic for the Balance Equation

JAN PAEGLE, JULIA N. PAEGLE AND GREGORY C. DODD

Department of Meteorology, University of Utah, Salt Lake City, UT 84112

(Manuscript received 14 July 1982, in final form 7 June 1983)

ABSTRACT

The origins of atmospheric states that are non-elliptic for the height constrained balance equation are examined from observational perspectives. Such states are commonly present in the deep tropics in objectively analyzed data sets. In order to analyze the source of this phenomenon, we compute terms of the divergence equation (from which the balance equation derives) for disturbed periods of the GATE experiment. Meaningful residuals cannot be obtained because they are obscured by observational uncertainty of the geopotential gradients that are calculated from the hydrostatic equation using temperature observations. The geopotential fields recomputed from the divergence equation using observed wind data appear to be much better determined, but they still produce fields that are non-elliptic for the height constrained nondivergent balance equation.

For the convective GATE cases, it appears that the essential balance of the divergence equation is between divergent accelerations, deforming accelerations, the divergent pressure force field and friction, while centripetal accelerations (including the Coriolis effect) are secondary. Thus, the underlying assumption of solenoidal flow in the balance equation is fundamentally wrong in regions of tropical convection. This appears to be the physical source of the poorly posed balance equation in many non-elliptic cases.

1. Introduction

It is well recognized that the accuracy of short-to-medium range weather prediction depends greatly upon initial conditions. The different observational densities and reliability of atmospheric variables necessitate the processing of observed data by objective analysis followed by an initialization step. Certain physical constraints (e.g., hydrostatic balance) between observed fields are applied at the objective analysis step, and others are applied at the initialization step.

The precise nature of the constraints is important in prediction with primitive equation models, since initial imbalances can propagate as spurious signals. In addition to the false excitation of small-scale gravity modes, improper initialization may also provoke larger scale error propagation.

A review of static initialization schemes based upon quasi-geostrophic theory is given by Bengtsson (1975). Implementation of such initialization procedures in quasi-geostrophic forecast models produces rather smooth synoptic-scale evolution because the geostrophic initialization procedure is entirely compatible with the quasi-geostrophic forecast algorithm.

The success of this procedure provides partial motivation for more recently proposed initialization techniques for the primitive equation models. These models govern low-frequency Rossby waves, as well as high-frequency gravity waves, which in the linear version are separable in terms of the frequency response of the normal modes of the governing equations. The projection of observed data only upon the low-frequency modes that carry most of the energy minimizes spurious excitation of gravity waves by poor data. Discussion of normal mode techniques is given by Dickinson and Williamson (1972), by Kasahara (1976), and others.

Extension to the complete nonlinear system that may also retain inhomogeneous forcing terms produces a number of practical difficulties. Nevertheless, considerable success with nonlinear model equations is reported in the studies of Baer and Tribbia (1977) and Machenhauer (1977). Leith (1980) relates these approaches to the quasi-geostrophic techniques.

A rather serious shortcoming to nonlinear normal mode initialization is the non-convergence of the numerical algorithms that are used to iterate upon the nonlinear terms. Daley (1978) and Tribbia (1981) point out that these problems are closely related to numerical difficulties that occur in the iterative solutions of the rotational wind from the height constrained balance equation when the latter becomes non-elliptic, (e.g., Charney 1955; Bolin 1955; Arnason, 1958; and others).

While unconstrained nonlinear normal mode initialization also has other difficulties that may lead to non-convergence, it is useful to understand the physical basis of the non-elliptic structures that are the source of the problem in the limit of height constrained initialization. This is the purpose of the present study.

Since the general normal mode approach is difficult to interpret on a local basis, we study the balancing implications of the divergence equation (from which the balance equation derives) in physical space (Section 2). This was also done by Kasahara (1982) using FGGE data. Sections 3 and 4 present regional diagnoses over the GATE experiments, and conclusions are summarized in Section 5.

2. Divergence equation

The divergence equation in spherical coordinates is

$$\underbrace{\frac{\partial D}{\partial t} + \underbrace{\frac{u}{a\cos\phi}\frac{\partial D}{\partial \lambda} + \frac{v}{a}\frac{\partial D}{\partial \phi}}_{\text{(b)}} + \omega\frac{\partial D}{\partial p}}_{\text{(a)}} + \underbrace{\tfrac{1}{2}(A^2 + B^2)}_{\text{(c)}} + \tfrac{1}{2}D^2 - \underbrace{\tfrac{1}{2}\xi^2}_{\text{(e)}} - \xi f + \mu D + \nabla^2\Phi$$

$$= \underbrace{-\beta u - \frac{u^2 + v^2}{a^2} - \frac{2\tan\phi}{a^2}\left[u\frac{\partial u}{\partial \phi} + v\frac{\partial v}{\partial \phi} + \frac{1}{\cos\phi}\left(u\frac{\partial v}{\partial \lambda} - v\frac{\partial u}{\partial \lambda}\right)\right]}_{\text{(h)}} + \underbrace{\frac{1}{a\cos\phi}\frac{\partial \omega}{\partial \lambda}\frac{\partial u}{\partial p} + \frac{1}{a}\frac{\partial \omega}{\partial \phi}\frac{\partial v}{\partial p}}_{\text{(j)}}, \quad (1)$$

where:

(λ, ϕ, a) (longitude, latitude, radius)

D divergence $\left\{= \frac{1}{a\cos\phi}\left[\frac{\partial}{\partial \phi}(v\cos\phi) + \frac{\partial u}{\partial \lambda}\right]\right\}$

A deformation rate $\left\{\frac{1}{a\cos\phi}\left[\frac{\partial v}{\partial \lambda} + \frac{\partial}{\partial \phi}(u\cos\phi)\right]\right\}$

B deformation rate $\left\{\frac{1}{a\cos\phi}\left[\frac{\partial}{\partial \phi}(v\cos\phi) - \frac{\partial u}{\partial \lambda}\right]\right\}$

ξ relative vorticity $\left\{\frac{1}{a\cos\phi}\left[\frac{\partial v}{\partial \lambda} - \frac{\partial}{\partial \phi}(u\cos\phi)\right]\right\}$

(u, v, ω) (zonal, meridional, vertical) motion

Φ geopotential height of pressure surface

f Coriolis parameter

β $\left[= \frac{1}{a}\frac{\partial f}{\partial \phi}\right]$

μ drag coefficient.

Pressure is used as the vertical coordinate, and friction is simplified in a drag formulation in term (f).

This formulation of friction is highly idealized with respect to the complex processes that actually occur in association with momentum mixing by deep convection. In particular, it may be inappropriate to apply a spatially uniform value. We use it because the available estimates of tropical dissipation times (Norquist *et al.*, 1977; Holton and Colton, 1972) are most directly translated into drag coefficients and because a much more detailed treatment may not be warranted if the sensitivity of results upon the values of μ is not excessive.

Many commonly used mass-flow balancing assumptions are derived from simplified forms of the divergence equation. For example, balance of the second term of (e) with (g) and (h) implies geostrophic vorticity. Balance of (c), (e), (g) and (h) leads to the nonlinear balance equation in the case of non-divergence. For purely rotational flows on the f-plane, this reduces to the gradient wind relation. Balance of (c) with (g) on a non-rotating plane represents potential flow (i.e., flow without absolute vorticity or divergence). As noted by Paegle and Paegle (1974), this is also a possible solution on the f-plane, depending upon the flow boundary conditions.

Locally balanced states that may evolve from (1) from initially unbalanced configurations are discussed by Paegle and Paegle (1974, 1976b, 1978), which are hereafter referred to as I, II, III. On the f-plane the *local* criterion for balanced stationary non-divergent flow (see II) is

$$\nabla^2\Phi + f^2/2 + (A_g^2 + B_g^2)/2 > 0 \quad (2)$$

(A_g and B_g are deformation rates of the geostrophic wind.) This criterion is somewhat different from that given as the ellipticity condition of the balance equation on the f-plane, i.e.,

$$\nabla^2\Phi + f^2/2 > 0. \quad (3)$$

Condition (3) reflects the character of the differential equation when its solution is inserted, while (2) reflects the physical realizability of the non-divergent solution from initially unbalanced states. Since (3) appears to distinguish convergence or non-convergence of iterative solution algorithms [see Tribbia (1981) for a recent global study], it is commonly used in operational work.

However, it is quite obvious that a realizability condition based upon the adjustment of transient solutions

toward steady state is a physically more reasonable constraint, and the mathematics of this approach are detailed in I, II, III. In particular, it is shown that in those instances when the non-divergent version of (1) produces a non-elliptic differential equation for the streamfunction, the time-dependent problem possesses a steady divergence limit for which the resulting equation is elliptic.

For the sake of clarity, the analysis demonstrating this is briefly repeated here. This analysis is based upon the divergence, vorticity and deformation equations, neglecting tilting terms associated with the horizontal variation of the vertical motion, as well as sphericity terms.

The resulting divergence equation is then

$$\frac{dD_s}{dt} = \tfrac{1}{2}[\eta^2 - (A^2 + B^2 + D^2)] - [\nabla^2\Phi + \tfrac{1}{2}f^2 - \tfrac{1}{2}\mu^2], \quad (4)$$

where:

$$D_s = D + \mu,$$

$$\frac{d}{dt} = \left(\frac{\partial}{\partial t} + \mathbf{V}\cdot\nabla + \omega\frac{\partial}{\partial p}\right),$$

$$\eta = \xi + f(\text{absolute vorticity}).$$

The deformation rate equations and the vorticity equation are:

$$\frac{dA}{dt} = -D_sA + f(B - B_g), \quad (5)$$

$$\frac{dB}{dt} = -D_sB + f(A - A_g), \quad (6)$$

$$\frac{d\eta}{dt} = -D_s\eta + \mu f. \quad (7)$$

Here A_g and B_g define geostrophic deformation rates. Equilibrium ($d/dt = 0$) solutions of (4)–(7) are easily obtained as

$$A = \frac{A_g - (D_sf^{-1})B_g}{1 + D_s^2f^{-2}}, \quad (8)$$

$$B = \frac{B_g + (D_sf^{-1})A_g}{1 + D_s^2f^{-2}}, \quad (9)$$

$$\eta = \mu f/D_s, \quad (10)$$

where D_s satisfies

$$\frac{(\mu f)^2}{D_s} - (D_s)^2 - \frac{A_g^2 + B_g^2}{1 + D_s^2f^{-2}} - (2\nabla^2\Phi + f^2) + \mu^2 = 0. \quad (11)$$

Eqs. (8)–(11) give valid steady limits of the time-dependent equations provided that the solutions are stable to small perturbations. Stability questions are discussed in II and III, and the selection of roots of (11) is discussed in III. The principal assumption of the stability analyses of I, II, III is uniformity of A_g, B_g, $\nabla^2\Phi$.

For present purposes, we note that even for the non-elliptic case

$$\nabla^2\Phi + f^2/2 < 0,$$

with $A_g = B_g = 0$ and $\mu = 0$, stable (realizable) solutions exist, and these display the divergence that solves (11) for that case. Upon the insertion of this divergence into the steady form of (4), the resulting (height and divergence constrained) balance equation is no longer hyperbolic for the streamfunction, even if the non-divergent version is hyperbolic. This alternative has also been suggested by Miyakoda (1956).

The applicability of this approach to real data is limited by the possibility of unstable solutions, and the assumptions of Lagrangian steady state [$(d/dt)(A, B, D, \eta) = 0$] as well as uniform A_g, B_g and $\nabla^2\Phi$. Therefore the legitimacy of the divergent flow remedies prescribed by Miyakoda (1956) and in I, II, III for non-elliptic data may be questioned (e.g., Tribbia, 1981). Nevertheless, non-elliptic geopotential configurations are commonly observed in the strongly divergent upper tropospheric flow above heavily convective disturbances (MacDonald 1977; Paegle and Paegle 1976a, 1978).

The next section presents detailed analyses of the complete divergence equation (1) and simplified diagnostic forms suggested in III, using the data of the GATE experiment in order to help resolve these questions.

3. GATE analysis

a. Data base and analysis

The data for this study were taken from the GATE quick-look analysis. From Phase II, ten observation times were taken from 4 August 1974 at 0000 GMT to 8 August 1974 at 1200 GMT. From Phase III, 20 observation times were selected from 2 September 1974 at 0000 GMT to 11 September 1974 at 1200 GMT. Both series were analyzed at 12 h intervals. The wind and height data were objectively interpolated to a 1° grid which extends over 4–36°W and over 1–17°N. This is described later.

The ships in the projects used three methods for taking upper air soundings (Houghton and Parker, 1974). The omega system, employing very low frequency radio signals, was used for determining wind speed and direction. Radiotheodolites and radar were used for wind speed and direction as well as for determining the heights.

Acheson (1974) summarized studies of the omega system's errors with respect to radar observations. In these cases, the root mean square (rms) errors range from 0.7 to 5.8 m s^{-1}. These values are dependent on the time averaging interval and on contamination

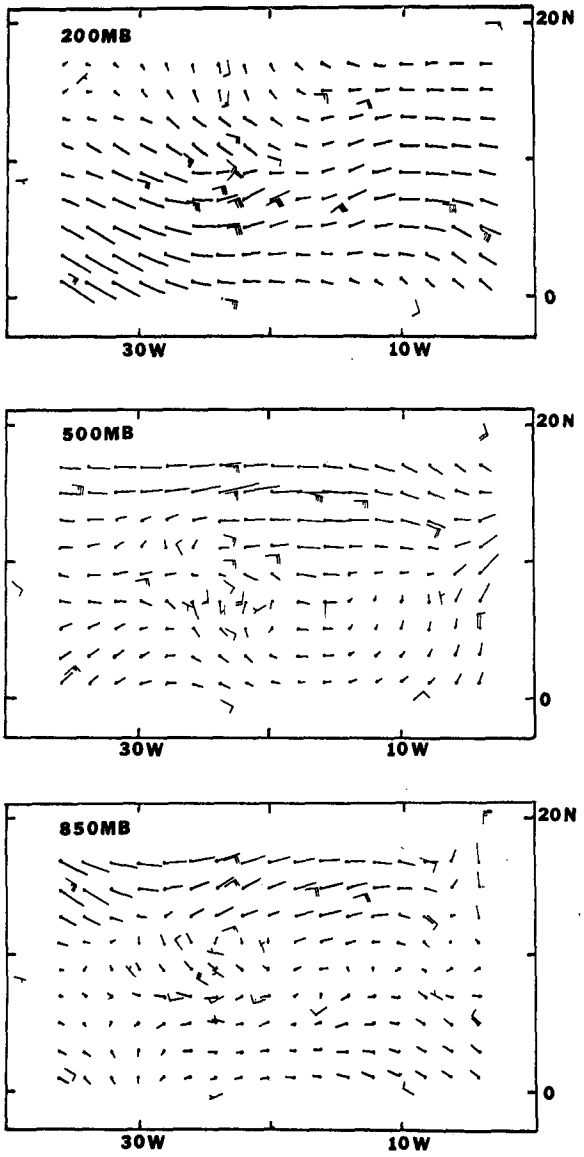

FIG. 1. Interpolated wind field on 2° grid for 1200 GMT 5 September 1974. Observations are shown as standard wind plots. Distance between grid points is 40 kt at 200 mb, 30 kt at 500 mb and 20 kt at 850 mb.

by poor data. Errors arise from phase error in the radio wave and from atmospheric interference. The errors in the wind measurements by the more standard procedures are due to errors in measuring ballon elevation and azimuth angles. Middleton and Spilhause (1953) indicated that at 5 km the wind direction may be in error by ±4° and the speed by ±2 m s^{-1}. At 200 mb (12.4 km) larger deviations are expected. The height errors result from errors in measuring the temperature and pressure. Lenhard (1973) determined that the standard deviation for the heights of the 200 mb surface is 11 m. Because the amplitude of the height gradient in the tropics is small, this error is quite critical.

The interpolation scheme used to generate grid point data for both the wind and height fields is a modification of a blending function interpolation in triangles as developed by Barnhill *et al.* (1973). Unlike many interpolation schemes used for meteorological purposes, this method makes no assumptions about the balance of forces in the atmosphere. It is also well suited for data which occur with varying densities. An example of an interpolated wind field is shown in Fig. 1.

b. Terms of the divergence equation

Figs. 2–9 illustrate the magnitude of all the terms [except b′ and j] in Eq. (1) as analyzed at 200 mb for 5 September at 1200 GMT. At this time a deeply convective system was moving across the GATE A–B array (see Fig. 10). Our analysis is based upon the raw quicklook data.

Suchman and Martin (1976) have also studied this case. They indicate that most of the cirrus level outflow occurs at ~250 mb. We assume that the vertical motion terms are small above 250 mb and omit them in our 200 mb calculations.

The results are plotted for an area (4–14°N, 7–33°W) which is slightly smaller than the full grid size. For consistency, the terms of the divergence equation and all other results (with the exception of the wind fields) are displayed in this manner. The geopotential

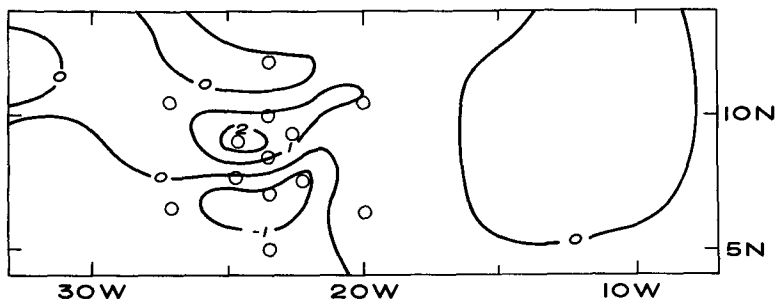

FIG. 2. Time-tendency term (10^{-9} s^{-2}) [term (a) in Eq. (1)]. Isopleths are at intervals of 10^{-9} s^{-2}. A–B scale ship network is indicated by open circles.

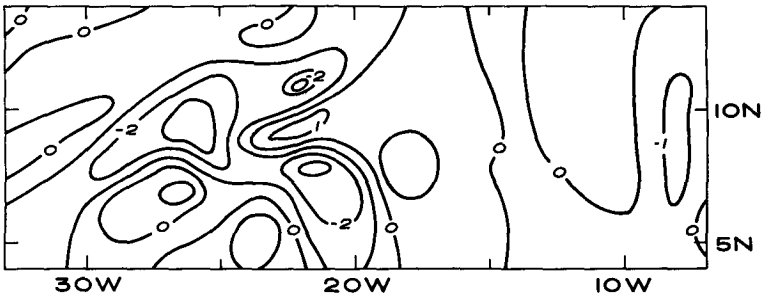

FIG. 3. Divergence advection term (10^{-9} s^{-2}), [term (b) in Eq. (1)]. Isopleths are at intervals of 10^{-9} s^{-2}.

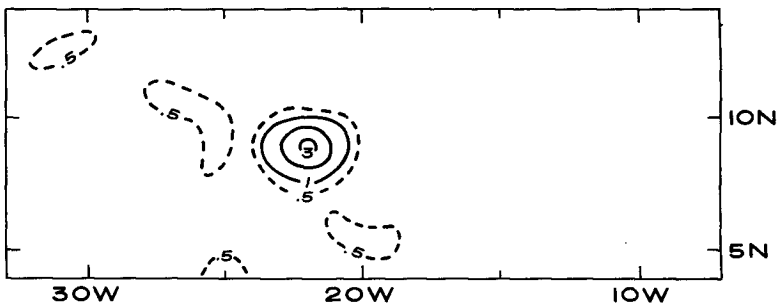

FIG. 4. Deformation term (10^{-9} s^{-2}) [term (c) in Eq. (1)]. Isopleths are at intervals of 10^{-9} s^{-2}.

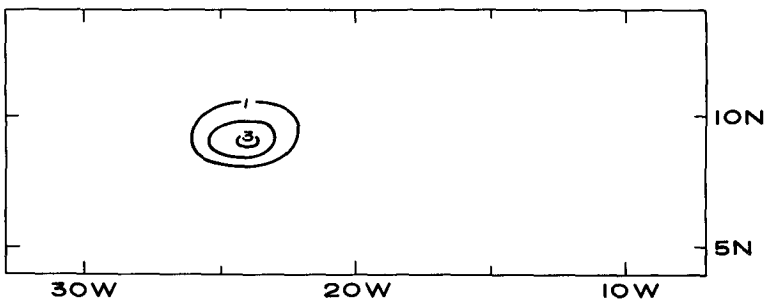

FIG. 5. Divergence term (10^{-9} s^{-2}) [term (d) in Eq. (1)]. Isopleths are at intervals of 10^{-9} s^{-2}.

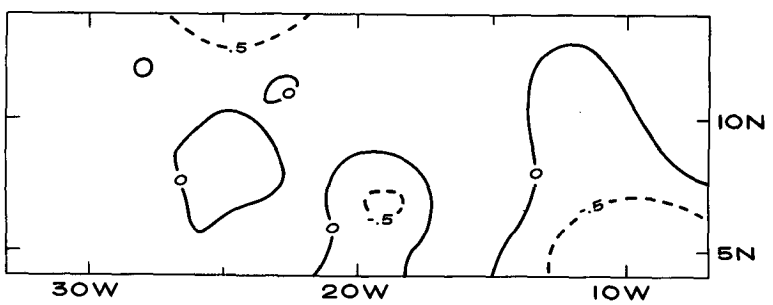

FIG. 6. Vorticity term (10^{-9} s^{-2}) [term (e) in Eq. (1)]. Dashed lines are at intervals 5×10^{-10} s^{-2}.

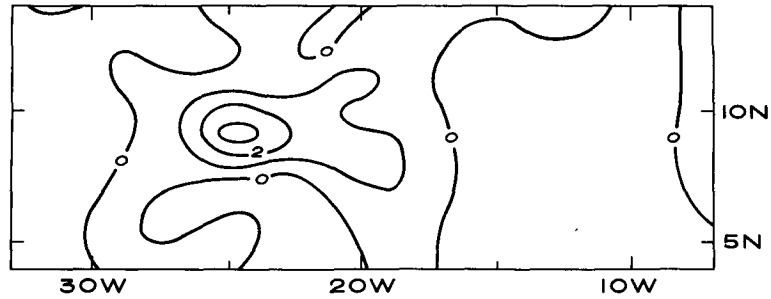

FIG. 7. Frictional term (10^{-9} s^{-2}) [term (f) in Eq. (1)]. $\mu = 4 \times 10^{-5}$ s^{-1}. Isopleths are at intervals of 10^{-9} s^{-2}.

term has the largest magnitude (10^{-9} s^{-2} to 10^{-8} s^{-2}, although the latter doesn't occur in the case shown). The metrical terms are on the order of 10^{-10} s^{-2}, and other terms possess magnitudes of the order 10^{-9} s^{-2}.

The magnitude of the friction term is dependent on the assumed drag coefficient. We select $\mu = 4 \times 10^{-5}$ s^{-1}, resulting in a friction term of order 10^{-9} s^{-2}. This rather large value of dissipation is necessary in order to maintain a consistent kinetic energy budget in the easterly flow of air from high to low pressure over the eastern Atlantic ocean.

In the present case, the geopotential height decreases by ~50 m from the eastern to the western boundary (Fig. 11), while the 200 mb easterly flow does not accelerate significantly between these boundaries. This typifies most cases, and a steady zonal momentum equation of the form

$$-fv = -\frac{\partial \Phi}{\partial x} - \mu u$$

requires values of $2\text{–}3 \times 10^{-5}$ s^{-1} for μ, if such changes of Φ are accurate.

These dissipation rates are somewhat larger than those found by Holton and Colton (1972) in association with the Asian monsoon, and by Norquist *et al.* (1977) in association with GATE wave composites. This may reflect stronger vertical momentum mixing by the rather active local convection of the present individual case.

From Figs. 2–9 it appears that simple mass-flow balancing is not possible. All diagnostic mass-flow balancing procedures neglect the divergence advection and most neglect the divergence tendency. These terms (Fig. 2, 3) are presently as large as terms that are commonly retained (e.g., the deformation term, Fig. 4). However, there is a certain degree of cancellation between advection and local tendency terms and the sum of terms (a)–(f) in the divergence equation (1) is generally dominated by contributions from the deformation term (Fig. 4), the divergence term (Fig. 5) and the friction term (Fig. 7), each of which has rather large positive values between 25 and 22°W at 9°N (centered over the convective disturbance).

The geopotential term (Fig. 8) is not in balance with the other terms. This may be because the variations of the geopotential values are obscured by observational error. The total observed variation in Fig. 11 between the closed high and low centers is only ~30 m. One positive error of 15 m and one negative error of −15 m could produce this result in a flat field. Since errors of this order probably occur in an observing system possessing 11 m standard deviation error, the interior details of Fig. 11 are rather questionable.

c. *Flow-consistent geopotential*

Eq. (1) can be solved for the geopotential field, given the wind field, by using the observed winds

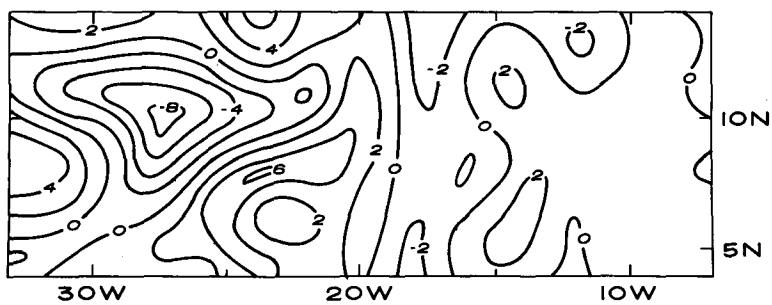

FIG. 8. Geopotential term (10^{-9} s^{-2}) [term (g) in Eq. (1)]. Isopleths are at intervals of 2×10^{-9} s^{-2}.

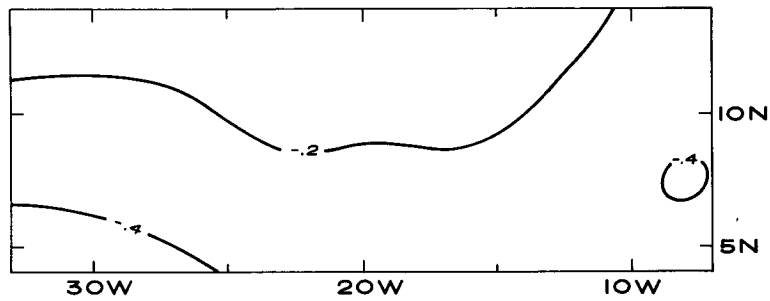

FIG. 9. Metrical terms (10^{-9} s^{-2}) [terms (h) and (i) in Eq. (1)]. Isopleths are at intervals of 0.2×10^{-9} s^{-2}.

within the domain and observed Φ on the domain boundary. The result is a geopotential field that is consistent with Eq. (1) and the observed wind field. Such a field may be more realistic than that calculated from the hydrostatic equation using observed temperatures if it does not deviate from the latter by more than expected observational errors. Results of Φ calculations based upon two different dissipation rates (μ) are displayed in Fig. 12. The results are quite insensitive to the value of μ. This insensitivity also characterizes other convectively active cases.

The relaxed height fields differ from observed height fields most substantially in the vicinity of the tropical wave. After performing similar analyses at 850 mb, we find thickness discrepancies between observed and relaxed height fields that are locally as large as 20–30 m between 850 and 200 mb. This corresponds to column-averaged temperature discrepancies that are locally as great as 1°C. Much of this difference is conceivably produced by typical temperature errors of radiosonde measurements, together with the obvious problems of securing representative data in sonde releases around deep convective clouds. Part of the discrepancy may also be related to wind data errors and interpolation uncertainty.

In order to estimate the sensitivity of the derived geopotential fields to observational and analysis uncertainties of the input wind field, we repeated the calculation of the geopotential from the divergence equation using two other analyses in the region centered upon the A–B scale array. One analysis is based upon time-filtered wind data, obtained directly from the quick-look radiosonde tabulation.[1] In the other case, the interpolated cloud motion vectors plotted in Fig. 4 of Suchman and Martin (1976) were used. In this case the grid-point values were tabulated directly from a photographic blow-up of Fig. 4 from Suchman and Martin (1976), using the given scale and measuring the vector magnitudes and direction manually.

Unlike the raw data, the time-filtered quick-look radiosonde data reduce the high-frequency contribution. Consequently, differences in the resultant geopotential field from that given in Fig. 12 represent sensitivity to data analysis. The cloud motion vector data taken from Suchman and Martin (1976) do not include radiosonde data and are based on cirrus level cloud motion. Therefore, differences in the resultant geopotential field from that obtained from the other calculations reflect sensitivity to observation type and elevation.

The divergence fields that result from each of these data sets are displayed in Fig. 13. The fields are rather similar in the region of strongest outflow with the peak values around 25°W, 9°N differing by less than 25%. It is not clear whether the presence of three small outflow centers in the cloud motion data is a consequence of better resolution or somewhat different elevation than 200 mb.

These sets of wind data were used in the calculation of geopotential fields from the divergence equation.[2] The solution of the Poisson equation for Φ is determined by the boundary conditions on Φ; together with the inhomogeneous term [left-hand side of Eq. (1)]. Since the geopotential boundary conditions are the same in each of the three cases, we display the sensitivity to the wind data by assuming uniform boundary conditions on Φ. The resulting geopotential fields (Fig. 14) are entirely associated with the motion field within the domain of integration. Although the patterns differ slightly in orientation and isopleth smoothness, there is a strong similarity in the three fields.

The cloud motion vector data give much more detail outside the region of the A–B scale radiosonde array (see top of Fig. 13). In addition to the two di-

[1] These data were taken from a preliminary analysis of Dr. K. V. Ooyama which filters frequencies higher than those of the semi-diurnal oscillation.

[2] In the case of the satellite cloud track winds, the time tendencies are computed using the analyses based upon the quick-look radiosonde data at 0000 GMT 5 September, and cloud track winds at 1200 GMT 5 September.

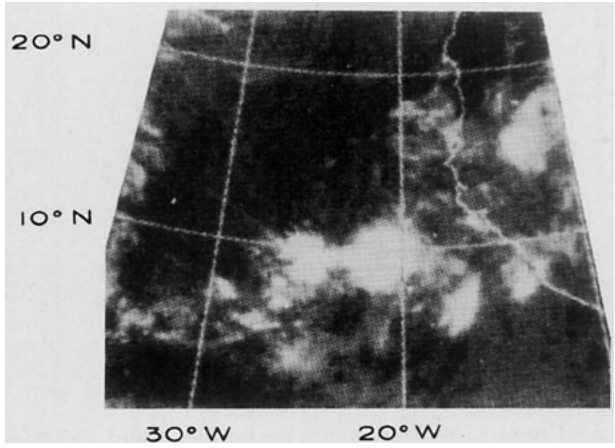

FIG. 10. SMS-1 visible image for 1230 GMT 5 September 1974.

vergence centers around the GATE data array, there appear three smaller areas of divergence maxima and minima outside this region that are eliminated by the smoothing inherent in the interpolation scheme used in the radiosonde analyses (middle and bottom of Fig. 13). The relative insensitivity of the geopotential field to these differences suggests that the latter field is mostly dominated by the larger scale structures of the disturbances. This well-known character of the solutions of the Poisson equation can be used to advantage when the major disturbances are co-located with the data-dense region (as in all present cases). The Appendix also indicates that the solutions are quite insensitive to typical boundary uncertainties.

We conclude that the geopotential field computed from the divergence equation using the observed wind field is much more reliably determined than is the geopotential field computed from the hydrostatic equation using the observed temperature field for these latitudes and scales. Thus, it is more appropriate to use the former in calculations requiring geopotential heights.

4. Consistency of diagnosed fields

The standard ellipticity criterion (3) computed from the geopotential fields of Fig. 12 is violated over most of the 7° × 5° longitude–latitude region centered upon 23°W, 9°N. In this section we present comparisons of diagnosed divergence fields suggested in III for such regions against kinematically computed divergence fields. Additionally, the vertical thermal structure of the flow-consistent Φ field is presented in order to compare its structure against other easterly wave diagnoses and to infer the thermal structure of the wave.

a. Diagnosed divergence field

Following III the steady divergence field (D_s) is computed from the solution of Eq. (11). In the process we used the recomputed geopotentials from the raw quicklook (time unfiltered) data. This is not merely a circular calculation because the deformation rate and the vorticity that are used in (11) are not the observed values but the solutions obtained from model equations (8), (9), and (10) using the recomputed Φ field, and assumptions outlined in Section 2.

If the balanced solutions of III are acceptable, D_s should be reasonably similar to observed divergences. Figs. 15–17 show examples of the observed and derived divergences, calculated using a drag coefficient of 4×10^{-5} s^{-1}. These times are during convectively disturbed episodes of phase III of the GATE experiment, and in all three cases the maximum diagnosed divergence is located within one grid point of the maximum observed divergence, and the peak values agree to within ~10–25%.

Thus, the diagnostic procedures are reasonably accurate in rather active transient easterly waves. Similarly good correspondence was found in other disturbed cases. We conclude that the assumptions used to obtain the steady states in Section 2 are appropriate to these cases.

b. Thermal structure

Using the derived heights at 200 and 850 mb, column-average temperatures were calculated from the integrated thickness equation

$$\bar{T} = [-\Delta\Phi/R \ln p]_{850}^{200},$$

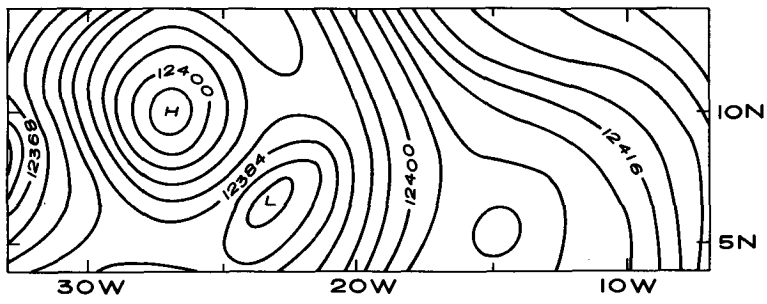

FIG. 11. Observed 200 mb height field at 1200 GMT 5 September 1974. Contour interval is 4 m.

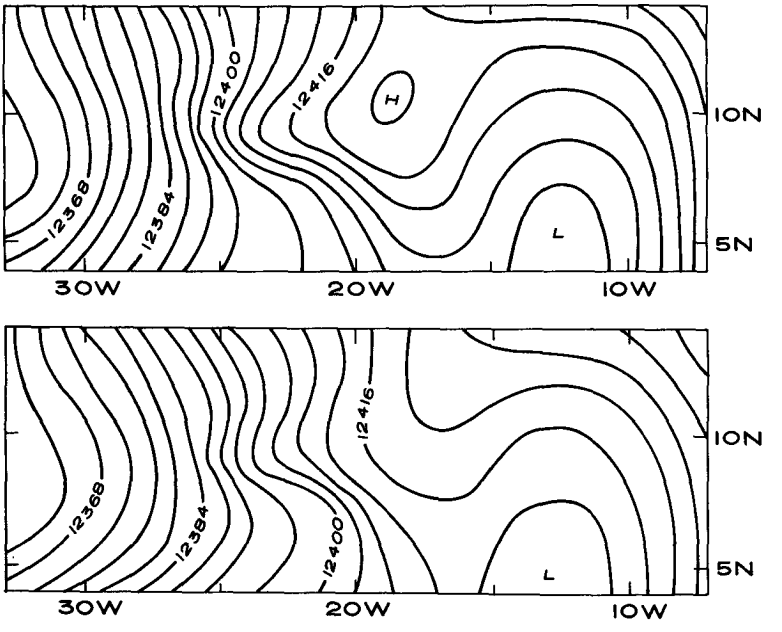

FIG. 12. Flow consistent height fields, at 200 mb computed from divergence equation using friction drag coefficient $\mu = 4 \times 10^{-5}$ s^{-1} (top) and 3×10^{-6} s^{-1} (bottom).

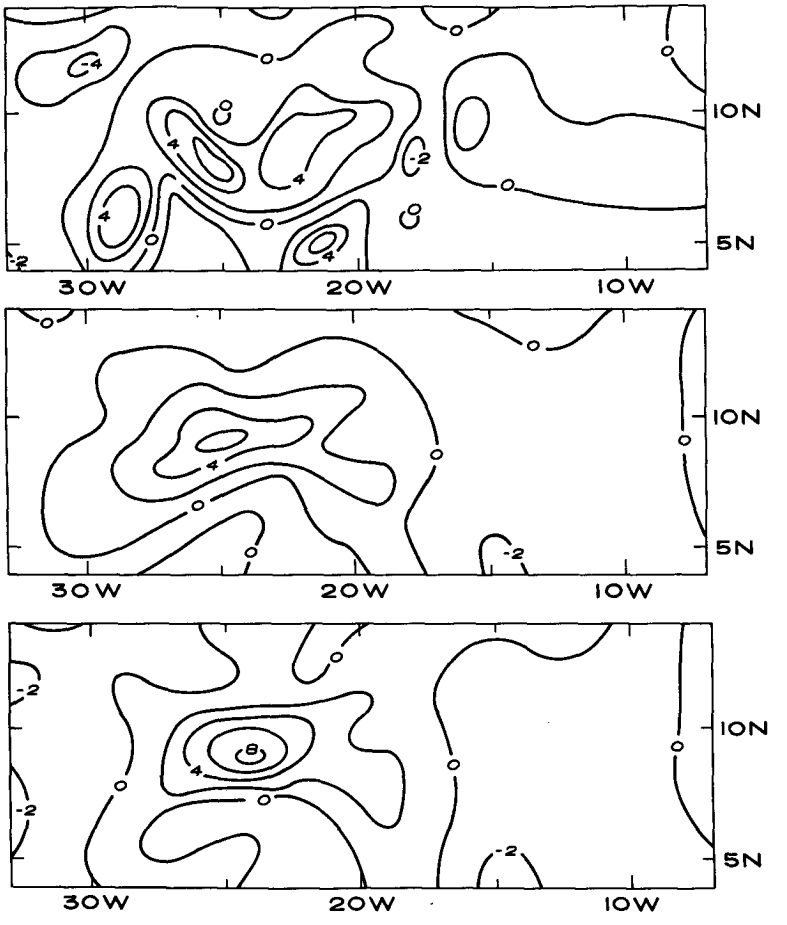

FIG. 13. Divergence at 200 mb computed from gridded cloud motion data (top), preliminary time-smoothed data of Dr. K. V. Ooyama (middle) and present analysis (bottom). The unit is 10^{-5} s^{-1}.

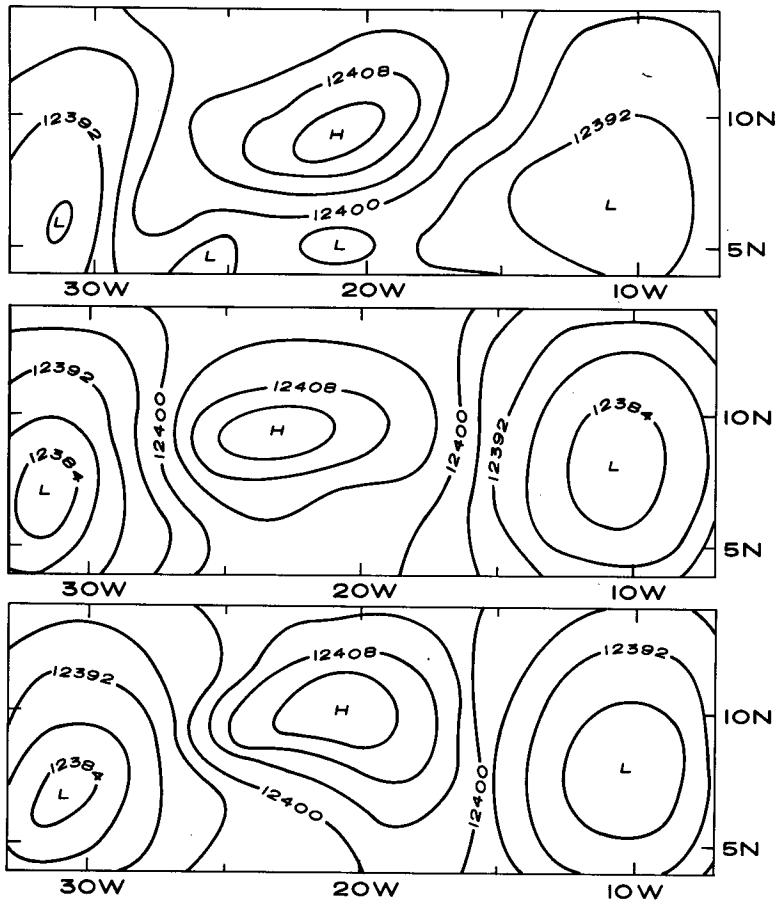

FIG. 14. Flow-consistent height fields computed from the divergence equation assuming uniform boundary conditions equaling 12 400 m at 200 mb. The top diagram utilizes cloud motion data, the middle diagram utilizes the time-smoothed wind data of K. V. Ooyama, and the bottom diagram is based on present analysis. The homogeneous boundary conditions are applied on latitude and longitude circles 3° outside the boundaries of Fig. 14.

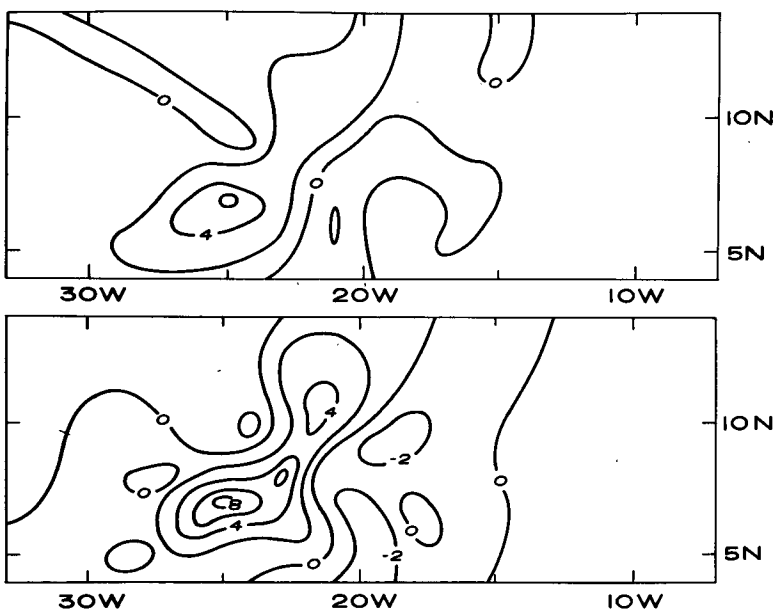

FIG. 15. Divergence at 200 mb computed from gridded wind data (top) and from diagnostic equation (4) using flow-consistent geopotential field (bottom) for 0000 GMT 3 September 1974. The unit is 10^{-5} s^{-1}.

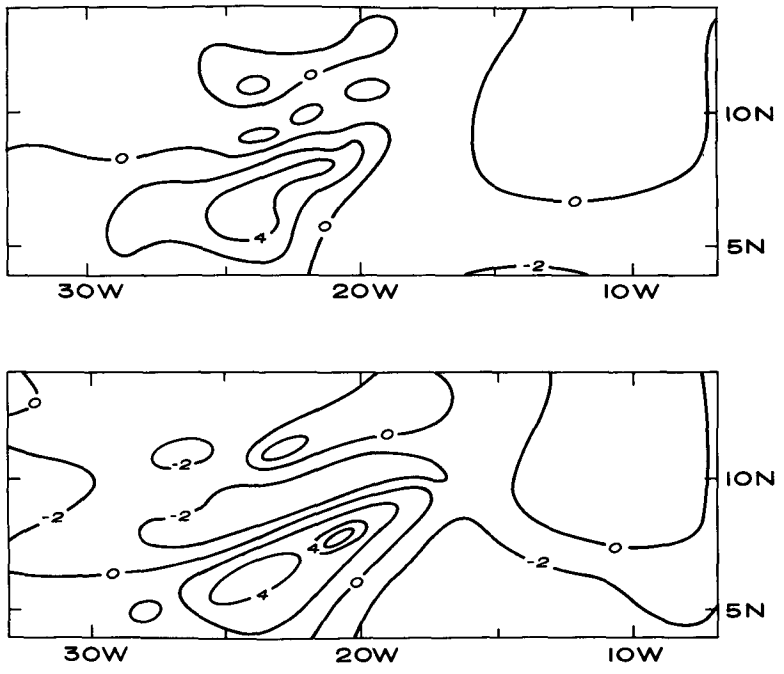

FIG. 16. As in Fig. 15 except for 0000 GMT 5 September 1974.

where R is the gas constant for dry air. Fig. 18 shows the temperature field implied by the heights of the 200 and 850 mb pressure surfaces for a composite of 24 convective times, centered around 700 mb vorticity maxima, during Phase III of GATE. The dominant characteristic of these fields is a thermal gradient pointing from the Atlantic Ocean toward Africa.

In order to assess whether the present structures resemble the composite easterly wave systems described by other investigators (e.g., Reed *et al.*, 1977), we have computed the geopotential and temperature fields associated exclusively with the field of motion within the domain of calculation by assuming homogeneous boundary conditions upon the geopoten-

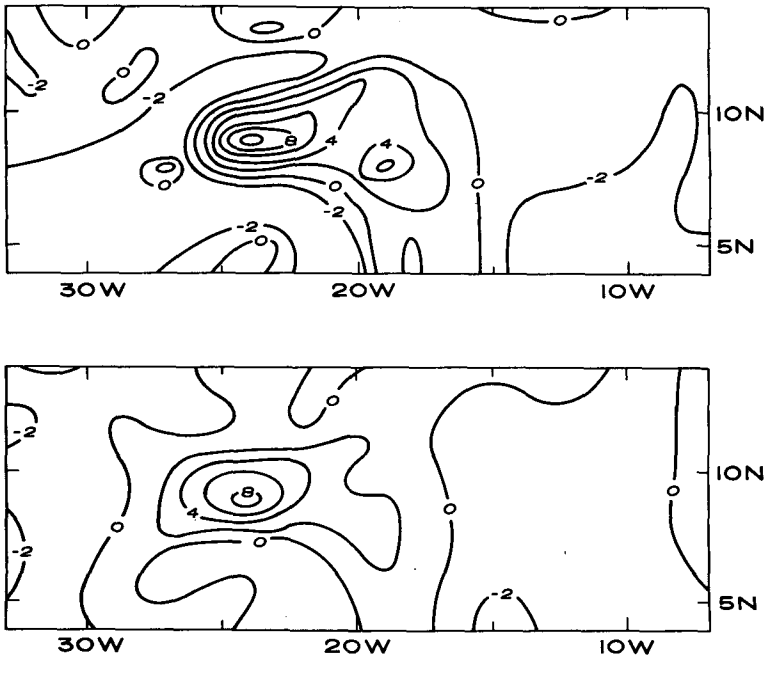

FIG. 17. As in Fig. 15 except for 1200 GMT 5 September 1974.

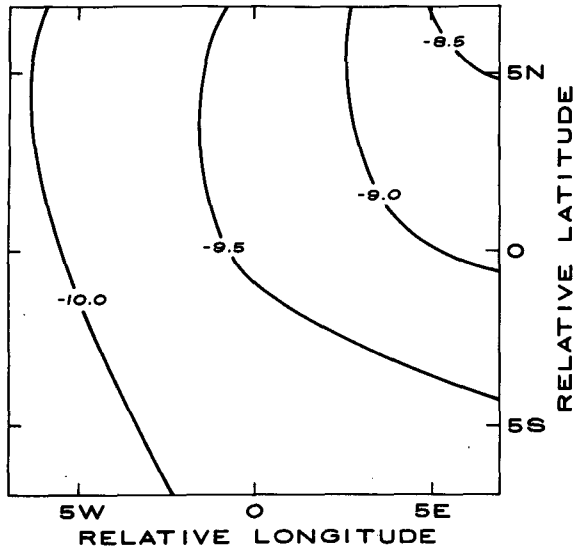

FIG. 18. Composited-column-averaged temperature (°C) computed from the 200 and 850 mb flow-consistent geopotential fields.

tial. The results may be considered as perturbations associated with the local motion field. The temperature perturbations related with the geopotential deviations in the 200–850 mb column thus computed are given by

$$T' = [-\Delta\Phi'/R \ln p]_{850}^{200},$$

where Φ' represents the geopotential deviations from the boundary value. If

$$\Phi'(200 \text{ mb}) > \Phi'(850 \text{ mb}),$$

a warm column is implied. Our composite (Fig. 19) indicates a positive temperature perturbation in the central region. The perturbations are generally less than 1°C. To provide a more complete description of the vertical structure of pressure, 500, 700 and 850 mb winds were used to obtain the corresponding perturbation height field for the composite of disturbed cases. These are shown in Fig. 20.

The composites clearly suggest a cold-core cyclone from ~500 mb downward, and a warm-core anticyclone above this. These fields are quite consistent with composites of easterly waves during GATE (Reed *et al.*, 1977). The positive thickness of the tropospheric column suggests local heating, possibly due to moist convection, and it is reasonable to speculate that heating, strong upper level divergence and non-elliptic domains are related.

5. Conclusions

The results of the present study show partial verification of conjectures presented in I, II, III, and MacDonald (1977) regarding the forcing by convective heating of circulations that are non-elliptic with regard to the balance equation.

In quasi-geostrophic motion for which the balance equation is elliptic, centripetal accelerations balance the convergence of the force field. In the cases of strong heating and related non-elliptic domains, it appears that the essential balance within the divergence equation is between divergent flow accelerations, centripetal accelerations and the divergence of the pressure force field. For the GATE cases, subgrid-scale drag is also important as suggested in III.

As shown by Kasahara (1982), the domain of ellipticity is quite distinct from that of realizability. In particular, the former is much more extensive. The present results support this conclusion for the relatively non-convective, non-elliptic regions of synoptic scale. However, in the locally convective domains of meso-to-synoptic scale, the divergence may be greater than or equal to the vorticity. This is different from Kasahara's (1982) conclusion, possibly because the structure functions of the ECMWF objective analysis scheme presume nondivergent flows in regions of this scale (Julian, 1981).

Stevens (1979) also finds that neither the quasi-geostrophic nor the balance approximations are valid for GATE composites. On the scale of the entire wave, his analyses suggest a prominent role for the local time-tendency term, and the rotational terms, and support the potential validity of linear models. The latter conclusions are at variance with present results because the nonlinear terms are rather smoothed in composited analysis over entire waves. Those studies do not resolve upper level outflow from individual squall lines (as is presently attempted).

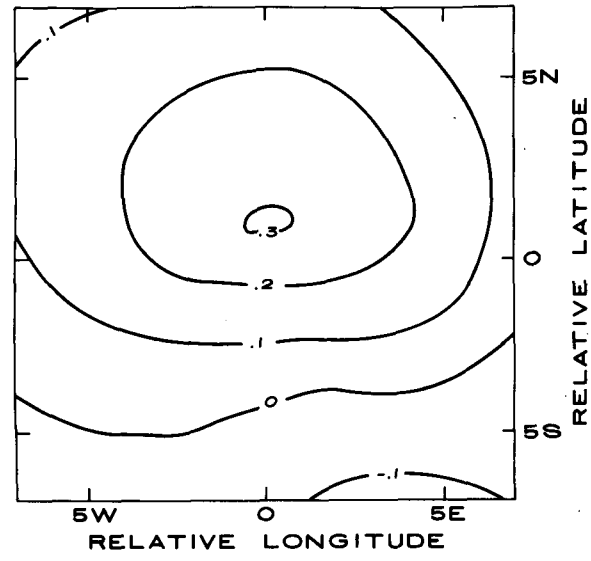

FIG. 19. As in Fig. 18, using height field obtained from the divergence equation assuming homogeneous boundary conditions. The homogeneous boundary conditions are applied on latitude and longitude circles 3° outside the boundaries of Fig. 14.

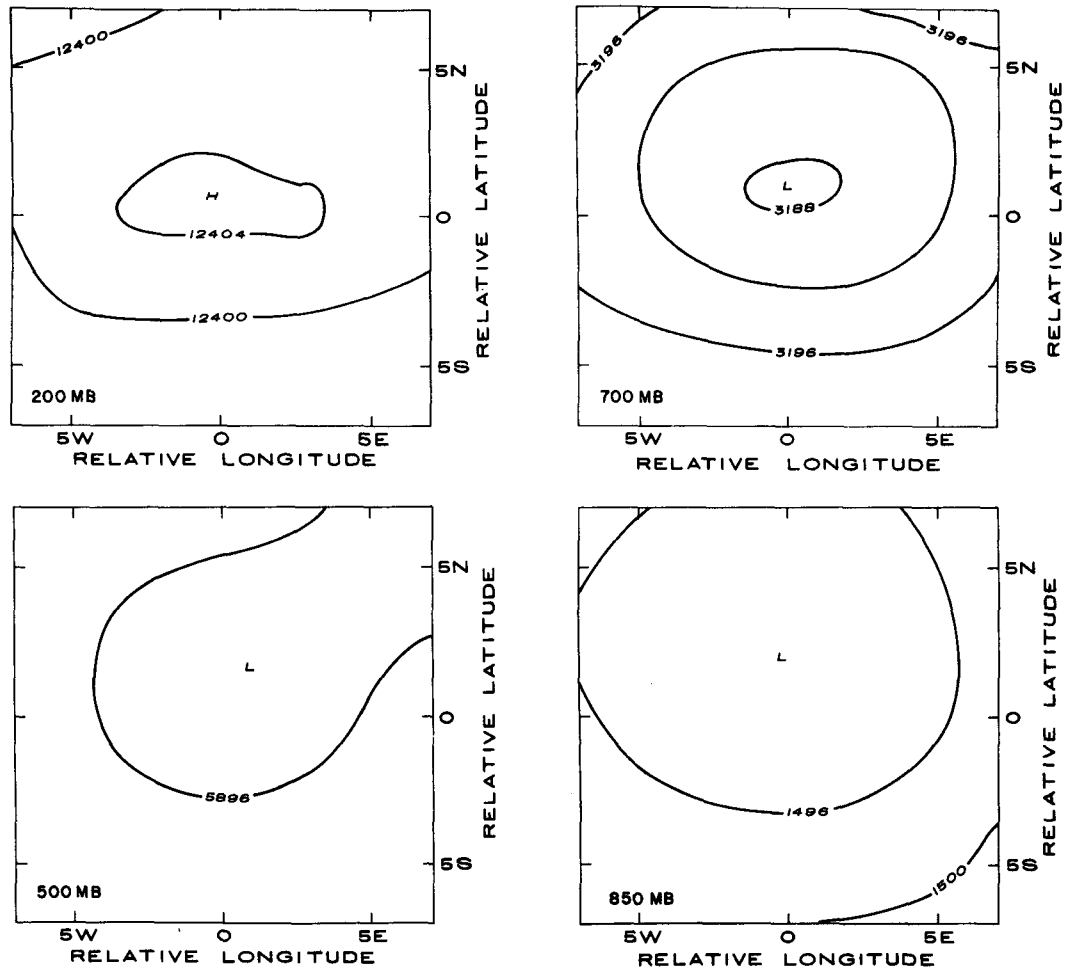

FIG. 20. Flow-consistent height fields of composite computed from divergence equation assuming uniform boundary conditions on height equaling 12 400 m at 200 mb (top, left); 5900 m at 500 mb (bottom, left); 3200 m at 700 mb (top, right); and 1500 m at 850 mb (bottom, right). The homogeneous boundary conditions are applied on latitude and longitude circles 3° outside the boundaries of Fig. 14.

Strongly divergent circulations are commonly noted in small-scale cumulus convection. Locally, these occur in those regions of the upper troposphere where deep cumulonimbus clouds deposit low-level air of high equivalent potential temperature as in the "hot tower" hypothesis of Riehl and Malkus (1958). The present results indicate that direct local over-turning may dominate rotational flow on scales as large as several hundred kilometers. These scales cannot be entirely parameterized as "subgrid" effects in most models, and may need to be explicity resolved.

To the extent that these patterns are important for the evolution of subsequent weather, it is essential to retain them in the initial fields of forecast models. Since height-constrained nonlinear initialization may not converge in such regions, it may be more practical to use wind observations and solve the divergence equation for the geopotential pattern (as in Section 3).

In addition to avoiding the convergence problems that often occur in height-constrained nonlinear initialization techniques, this approach is also consistent with the theory of geostrophic adjustment for most scales in the deep tropics, and for mesoscales in higher latitudes. The geopotential field adjusts to the wind field in such cases (Phillips, 1963; Blumen, 1972). Because of this, a forecast utilizing both wind and height data in these regions would quickly adjust toward consistency with the wind data.

This approach also retains some problems that require further study. The geopotential data must be given on lateral boundaries. We have tested the impact of typical boundary value uncertainties upon the interior geopotential field and, as suggested by the analysis given in the Appendix, the impact of these upon the interior field is rather slight.

A potentially greater difficulty concerns the relative importance of friction. The present results are not

excessively sensitive to the selection of the drag coefficient because the sum of the divergence and deformation terms dominates the friction term around the center of the disturbance (compare Figs. 4 and 5 with Fig. 7). However, the drag term is presently larger than the rotational term (Fig. 6). Because of this, the results for less convective cases, characterized by smaller divergence and deformation, may be more sensitive to *ad hoc* treatments of momentum mixing with simple drag coefficients. We are continuing to study the extent to which the apparent friction reflects actual mechanical dissipation and not merely a lack of resolution of smaller scale, high-frequency oscillations.

For large forecast domains, it is desirable to utilize both temperature and wind observations. In these cases, nonlinear equations and iterative solution techniques may be unavoidable for the initialization, and further work is needed to overcome the problems described in the Introduction.

Acknowledgments. This work was begun in 1977 during a visit of the authors to the Advanced Study Program at NCAR, which is supported by the National Science Foundation. We are grateful for access to the GATE analyses of K. V. Ooyama, and for constructive criticisms of the manuscript by A. Kasahara. The research has also been supported by NSF Grants ATM-77-17349 and jointly by the National Science Foundation and the National Oceanic and Atmospheric Administration under Grant ATM-8018158 to the University of Utah. Ms. A. Johnson and Mrs. R. L. Rhodes typed the manuscript.

APPENDIX

Boundary Effects

The solutions of the geopotential field depend upon the imposed boundary conditions. In this Appendix we describe the sensitivity of the flow-consistent Φ field to the uncertainty inherent in boundary data upon Φ. The latter are based upon the temperature observations and the hydrostatic solution for Φ. This calculation produces geopotential height errors on the order of ± 10 m in the troposphere. Unless such errors damp rapidly with increasing distance from the boundaries, the flow-consistent geopotential structure of Fig. 14 would be seriously degraded.

Rather than displaying many individual sensitivity tests (that support the subsequent general analysis) we study this problem in general terms.

For the general treatment we require the solution to two problems:

$$\nabla^2\Phi = F_1, \tag{A1}$$

with $\Phi = \Phi_1$ on boundaries, and

$$\nabla^2\Phi = F_2, \tag{A2}$$

with $\Phi = \Phi_2$ on boundaries. Here F_1 and F_2 represent all terms of Eq. (1) that can be specified from wind observations.

The wind observations within the boundaries can be perturbed by the typical observational uncertainty while leaving the Φ observations fixed on the boundaries (i.e., $F_1 \neq F_2$, but $\Phi_1 = \Phi_2$). This was done in Section 3c in order to study the impact of wind observational uncertainty upon the solution of Φ.

Presently, we set $F_1 = F_2$ and investigate the impact of changing boundary data ($\Phi_1 \neq \Phi_2$). Subtracting (A2) from (A1) we obtain

$$\nabla^2\Phi = 0, \tag{A3}$$

as the equation governing the interior perturbation Φ with

$$\Phi = \Phi_1 - \Phi_2 \text{ on boundaries.}$$

Eq. (A3) is most easily solved in a cylindrical geometry (r, λ), where r is the radial distance from the origin, and λ is azimuth angle. We assume that the azimuthal dependence of the boundary values at a bounding radius (normalized to 1 for simplicity) is given in a Fourier series of the form

$$(\Phi_1 - \Phi_2)(r = 1, \lambda) = \sum_{m=0}^{M} A_m e^{im\lambda}. \tag{A4}$$

The maximum number of modes (M) would be approximately equal to half the number of geopotential observations that are used for boundary values.

For each mode m, a solution of (A3) of the form

$$\Phi_m = A_m r^m e^{im\lambda}, \tag{A5}$$

satisfies (A3), so that the total solution is

$$\Phi(r, \lambda) = \sum_{m=0}^{M} A_m r^m e^{im\lambda}. \tag{A6}$$

If the squared standard deviation of observation error on the boundary represents the variance of $\Phi_1 - \Phi_2$, we have

$$\sum_{m=1}^{M} A_m^2 \approx (10\text{m})^2 g^2 \tag{A7}$$

on the boundaries.

From solution (A6) it is clear that the variance of mode m, associated with the erroneous boundary values, decreases as $(A_m r^m)^2$ with decreasing r (i.e., at least as fast as r^2 for all modes except the azimuthal average $m = 0$).

Therefore, the error contribution from boundary errors to the horizontally variable portion of the geopotential height field are likely to be only a few meters or less, halfway between the center of the grid and the boundary. In the case that many geopotential height observations (possessing random errors with standard deviation of ~ 10 m) are available, the rel-

ative contribution of the lowest azimuthal wave mode ($m = 1$) becomes less important than the contribution of higher modes ($m > 1$) that damp much more quickly with distance from the boundary. In such instances the error is considerably less than a few meters at distances midway between the grid center and the boundary.

REFERENCES

Acheson, D. T., 1974: Omega windfinding and GATE. *Bull. Amer. Meteor. Soc.*, **55,** 385–398.

Arnason, G., 1958: A convergent method for solving the balance equation. *J. Meteor.*, **15,** 220–225.

Baer, F., and J. J. Tribbia, 1977: On complete filtering of gravity modes through nonlinear initialization. *Mon. Wea. Rev.*, **105,** 1536–1539.

Barnhill, R. E., G. Birkhoff and W. J. Gordon, 1973: Smooth interpolation in triangles. *J. Approx. Theory,* **8,** 114–128.

Bengtsson, L., 1975: Four-dimensional assimilation of meteorological observations. GARP Publ. Ser., No. 15, Global Atmospheric Research Programme, WMO-ICSU Joint Organizing Committee, Geneva, 76 pp.

Blumen, W., 1972: Geostrophic adjustment. *Rev. Geophys. Space Phys.*, **10,** 485–528.

Bolin, B., 1955: Numerical forecasting with the barotropic model. *Tellus,* **7,** 27–49.

Charney, J., 1955: The use of the primitive equations of motion in numerical prediction. *Tellus,* **7,** 22–26.

Daley, R., 1978: Variational non-linear normal mode initialization. *Tellus,* **30,** 201–218.

Dickinson, R. E., and D. L. Williamson, 1972: Free oscillations of a discrete stratified fluid with application to numerical weather prediction. *J. Atmos. Sci.*, **29,** 623–640.

Holton, J. R., and D. E. Colton, 1972: A diagnostic study of the vorticity balance at 200 mb in the tropics during the northern summer. *J. Atmos. Sci.*, **30,** 1287–1302.

Houghton, D. D., and D. E. Parker, 1974: *The Synoptic-Scale Sub-Programme for the* GARP *Atlantic Tropical Experiment.* World Meteorological Organization, 105 pp.

Julian, P. R., 1981: The tropical observing systems in FGGE: An analysis of results. *Proc. Int. Conf on Early Results of* FGGE *and Large Scale Aspects of its Monsoon Experiments,* Geneva, WMO, 2.2–2.9.

Kasahara, A., 1982: Significance of non-elliptic regions in balanced flows of the tropical atmosphere. *Mon. Wea. Rev.*, **110,** 1956–1967.

——, 1976: Normal modes of ultra-long waves in the atmosphere. *Mon. Wea. Rev.*, **104,** 669–690.

Leith, C. E., 1980: Nonlinear normal mode initialization and quasi-geostrophic theory. *J. Atmos. Sci.*, **37,** 958–968.

Lenhard, R. W., 1973: A revised assessment of radiosonde accuracy. *Bull. Amer. Meteor. Soc.*, **54,** 691–693.

MacDonald, A. E., 1977: On a type of strongly divergent steady state. *Mon. Wea. Rev.*, **105,** 771–785.

Machenhauer, B., 1977: On the dynamics of gravity oscillations in a shallow-water model, with applications to normal mode initialization. *Beitr. Phys. Atmos.*, **50,** 253–271.

Middleton, W. E. K., and A. F. Spilhause, 1953: *Meteorological Instruments.* University of Toronto Press, 286 pp.

Norquist, D. C., E. E. Recker and R. J. Reed, 1977: The energetics of African wave disturbance as observed during Phase III of GATE. *Mon. Wea. Rev.*, **105,** 334–342.

Paegle, J. 1978: The transient mass-flow adjustment of heated atmospheric circulations. *J. Atmos. Sci.*, **35,** 1678–1688.

——, and J. N. Paegle, 1974: An efficient and accurate approximation to the balance wind with application to non-elliptic data. *Mon. Wea. Rev.*, **102,** 838–846.

——, and ——, 1976a: On geopotential data and ellipticity of the balance equation: A data study. *Mon. Wea. Rev.*, **104,** 1279–1288.

Paegle, J. N., and J. Paegle, 1976b: On the realizability of strongly divergent supergradient flows. *J. Atmos. Sci.*, **33,** 2300–2303.

——, and ——, 1978: Frictional effects in strongly divergent flows. *J. Atmos. Sci.*, **35,** 1197–1203.

Phillips, N. A., 1963: Geostrophic motion. *Rev. Geophys.*, **6,** 123–176.

Reed, R. J., D. C. Norquist and E. E. Recker, 1977: The structure and properties of African wave disturbances as observed during Phase III of GATE. *Mon. Wea. Rev.*, **105,** 317–333.

Riehl, H., and J. Malkus, 1958: On the heat balance of the equatorial trough zone. *Geophysica,* **6,** 503–535.

Stevens, D. E., 1979: Vorticity, momentum and divergence budgets of synoptic-scale wave disturbances in the tropical eastern Atlantic. *Mon. Wea. Rev.*, **107,** 535–550.

Suchman, D., and D. Martin, 1976: Wind sets from SMS images: An assessment of quality for GATE. *J. Appl. Meteor.*, **15,** 1265–1278.

Tribbia, J. J., 1981: Nonlinear normal mode balancing and the ellipticity condition. *Mon. Wea. Rev.*, **109,** 1751–1761.